

Non-fluorinated Zinc Anions: A Low-Cost Environmental Approach for Reversible Zinc Electrochemistry

Mega Kar,^[a] The An Ha,^[a] Dale Duncan,^[b] Fangfang Chen,^[a] Pavel Cherepanov,^[b] Ju Sun,^[a] and Cristina Pozo-Gonzalo^{*[a]}

Rechargeable zinc batteries (RZBs) are of immense interest as low-cost and sustainable energy storage devices. However, formation of Zn dendrites, Zn corrosion, and undesired side reactions in aqueous electrolytes as well as the use of costly fluorinated salts in organic electrolytes, have hindered the commercialization of RZBs. In this work, a cost-efficient and environmentally friendly, non-aqueous electrolyte comprised of zinc dicyanamide ($\text{Zn}(\text{dca})_2$) in dimethyl sulfoxide (DMSO) is shown to support the electrochemical cycling of zinc. Fourier-transform infrared (FT-IR) spectroscopy complemented with theoretical studies suggest that the solvation of Zn^{2+} is stabilized with both $[\text{dca}]^-$ anions and DMSO molecules at high

concentrations ($\geq 1.0 \text{ M}$) of the zinc salt content. Stable charge/discharge cycles in zinc symmetrical cells with low overpotentials (0.05 V) were especially observed for 1.0 M $\text{Zn}(\text{dca})_2/\text{DMSO}$ over 90 cycles at 1.0 mA cm^{-2} with scanning electron microscopy (SEM) images confirming the formation of a dense and smooth zinc morphology on metal anode surface post-cycling. X-ray photoelectron spectroscopy (XPS) also shows that the presence of zinc nitride (Zn_3N_2) helps form a stable SEI layer in the presence of 1.0 M and 2.5 M systems, making [dca]-based electrolytes highly promising candidates in rechargeable zinc batteries.

Introduction

Although lithium-ion technology has garnered immense interest as rechargeable batteries to maximize the usage of renewable energy, the high reactivity of lithium (Li) metal, together with the scarcity, toxicity and unethical extraction of the active materials used in the cathode raises questions as a sustainable emerging energy storage. On the contrary, low-cost, and safe energy storage technologies such as rechargeable zinc batteries (RZBs) hold great promise for the near future. Zinc metal is highly abundant and cheap and while it has a high theoretical specific (820 mAh g^{-1}), its volumetric capacity is much higher than Li metal (5855 mAh cm^{-3} for Zn vs. 2062 mAh cm^{-3} for Li). Such features make zinc very appealing including rechargeable zinc-air which have very high theoretical energy density ($1,218 \text{ Wh kg}^{-1}$ vs. LiB $\leq 350 \text{ Wh kg}^{-1}$).

Although RZBs such as $\text{Zn}-\text{MnO}_2$ are commercially available, they are not widely implemented and completely missing

for applications in stationary energy storage.^[1] One of the main challenges in pursuing RZBs is finding appropriate electrolytes that allows long-term Zn metal cycling. The use of alkaline electrolytes in these batteries, which is highly unstable to both the cathode and anode, results in limited capacity and poor cycle life (≤ 30 cycles),^[2] and the main technological limitations are the formation of irreversible Zn(OH)_2 and ZnO , as well the presence of zinc dendrites. Mildly acidic aqueous electrolytes have also been investigated in improving the cycle life of metallic Zn^[3] but Zn corrosion, passivation, dendrite formation and hydrogen evolution upon charging of the battery still remain a concern.^[4] Hydrogen evolution has been recently tackled by introducing certain “water-in-salt” (WISE) electrolytes such as $1 \text{ m (mol kg}^{-1}\text{)} \text{ Zn(TFSI)}_2 + 20 \text{ m (mol kg}^{-1}\text{)} \text{ LiTFSI}$, in which most of the water molecules are solvated to zinc, demonstrating long-term cycling of zinc (>4000 cycles at 50 mA g^{-1} , 1000 mAh g^{-1}) and delivering an energy density of 180 Wh kg^{-1} .^[5] Nevertheless, such aqueous electrolytes are highly corrosive making them unfeasible in practical applications and require super-concentrated fluorinated lithium and zinc salts^[6] which are costly and raises environmental concerns. Other ways to limit hydrogen evolution reaction and zinc-dendrite formation has recently been shown by Chen et al.^[7] and others^[8] using dual-salt based electrolytes as well as organic additives in aqueous systems, which result in the formation of a stable electrolyte/electrode zinc interphase and long-term electrochemical cycling of zinc.

On the other hand, non-aqueous electrolytes offer many advantages including a wider electrochemical window^[9] and the absence of the hydrogen evolution reaction. A few efforts have been made using acetonitrile and propyl carbonate,^[10] mixed with zinc tetrafluoroborate $[\text{Zn}(\text{BF}_4)_2]$,^[11] zinc di-

[a] Dr. M. Kar, Dr. T. A. Ha, Dr. F. Chen, Dr. J. Sun, Ass. Prof. C. Pozo-Gonzalo
Institute for Frontier Materials (IFM)
Deakin University
Burwood Campus, Burwood 3125, Victoria, Australia
E-mail: m.kar@deakin.edu.au
cpg@deakin.edu.au

[b] D. Duncan, Dr. P. Cherepanov
School of Chemistry
Monash University
Clayton 3800, Victoria, Australia

 Supporting information for this article is available on the WWW under
<https://doi.org/10.1002/batt.202200412>

 © 2022 The Authors. *Batteries & Supercaps* published by Wiley-VCH GmbH.
This is an open access article under the terms of the Creative Commons Attribution License, which permits use, distribution and reproduction in any medium, provided the original work is properly cited.

[bis(trifluorosulfonyl)imide] $[\text{Zn}(\text{OTf})_2]$ ^[12] and zinc di-[bis(trifluoromethanesulfonyl)imide] $[\text{Zn}(\text{TFSI})_2]$.^[13] For instance, the use of $\text{Zn}(\text{OTf})_2$ in trimethyl phosphate (TMP)^[10] with the addition of dimethyl carbonate (DMC)^[14] led to a dendrite-free morphology of zinc deposits stable electrochemical cycling of Zn over 5000 h with a CE of 99.15%. The use of $\text{Zn}(\text{OTf})_2$ in dimethylformamide (DMF)^[15] with the addition of Cu^{2+} ions as an additive has also demonstrated electrochemical long-term stability of zinc (>1400 h) at high current densities ($5.0 \text{ mA cm}^{-2}/5.0 \text{ mAh cm}^{-2}$) in a $\text{Zn}|\delta\text{-MnO}_2$ cell.^[16]

With the purpose of designing stable, low-cost and environmentally friendly materials, this work investigates an organic electrolyte comprised of non-fluorinated electrolyte, zinc dicyanamide $[\text{Zn}(\text{dca})_2]$ in dimethyl sulfoxide (DMSO). DMSO is highly appealing as a battery electrolyte due to its high dielectric constant ($\epsilon=46.45$), high flash point (95 °C at 1 atm), and low toxicity. According to the material safety data sheet (MSDS), in comparison to organic solvents currently studied in the literature for rechargeable zinc batteries, i.e., DMF^[16] and trialkylphosphates,^[12d] DMSO has a higher half maximal effective concentration ($\text{EC}_{50}=24,600 \text{ mg/L}$ vs. 13,100 mg/L and 900 mg/L for DMF and triethylphosphate respectively). The use of DMSO as an electrolyte additive in aqueous electrolytes has also shown to suppress the formation of zinc dendrites in aqueous Zn-ion batteries.^[17] Additionally, $\text{Zn}(\text{dca})_2$ is moisture-stable, non-fluorinated and easily designed from a one-pot synthetic step using low-cost precursors (see Experimental Section). To date, this zinc salt coupled with DMSO is the most cost-efficient and safe organic electrolyte investigated for reversible zinc electrochemistry. Table S1 summarizes the cost and the toxicity of various organic electrolytes reported for electrochemical cycling of zinc.

Previous work by Simons et al. demonstrated a $\text{Zn}|\text{Zn}$ symmetric cell in the presence of $\text{Zn}(\text{dca})_2$ in the ionic liquid $[\text{C}_2\text{mim}][\text{dca}]$ (where $\text{C}_2\text{mim}=1\text{-ethyl-3-methylimidazolium}$) as the electrolyte, cycled over 95 cycles at 0.1 mA cm^{-2} with overpotentials $\geq \pm 0.1 \text{ V}$.^[18] A full battery $\text{Zn}-\text{poly}(3,4\text{-ethylenedithiophene})$ (PEDOT) battery was cycled over 320 cycles at 15 mA g^{-1} . However, a capacity decay of 52% was observed shortly after 200 cycles in the $\text{Zn}|\text{PEDOT}$ cell. The sluggish diffusion of Zn^{2+} ions in a highly viscous ionic liquid was also predicted to be the cause of cell polarization.

In this paper, by replacement of the ionic liquid with a low viscous organic solvent such as DMSO, high concentration of zinc [up to 2.5 M $\text{Zn}(\text{dca})_2$] was achieved which are highly desirable in increasing the transference number of metal ions and thereby cycling batteries at high current densities, as demonstrated by Forsyth et al.^[19] Previously the electrochemical reversibility of zinc in DMSO at low concentration of the zinc salt, 0.25 M $\text{Zn}(\text{OTf})_2$, was achieved resulting in slower kinetics of Zn^{2+} ions at the metal interface and high overpotentials (approximately 100 mV at 1 mA cm^{-2}). Although the electrolyte showed potential application in a rechargeable $\text{Zn}-\delta\text{-MnO}_2$ battery, there is a lack of information in the literature on the underlying mechanisms,^[12a] such as the solvation of zinc in non-aqueous electrolytes, that govern the electrochemical performance of zinc.

Herein we investigate the electrochemical cycling behaviour of zinc in DMSO in the presence of 0.5 M, 1.0 M and 2.5 M $\text{Zn}(\text{dca})_2$. FT-IR spectroscopy and MD simulation studies suggest that there is an optimum solvation of Zn^{2+} in which both the DMSO and dca molecules coordinate with Zn^{2+} and the existence of free DMSO in solution. Moreover, a smooth, non-dendritic morphology of zinc is also achieved post symmetric cell cycling with XPS further showing the presence of conductive zinc nitride species on the surface of the zinc interface in the higher concentrated systems (1.0 M and 2.5 M $\text{Zn}(\text{dca})_2/\text{DMSO}$). The presence of such fluorine-free, nitride-rich species in creating a stable solid electrolyte zinc interface creates a major breakthrough in the field of non-aqueous zinc electrolytes for RZBs, in which zinc fluoride-rich morphology has been previously postulated to be a source of a stable SEI layer on the zinc anode.^[11,20]

Experimental Section

Material

Zinc nitrate hexahydrate ($\text{Zn}(\text{NO}_3)_2 \cdot 6\text{H}_2\text{O}$, 98%, Sigma Aldrich), sodium dicyanamide [$\text{Na}(\text{dca})$, 96%, Sigma Aldrich] were used as received. The synthesis of zinc dicyanamide $[\text{Zn}(\text{dca})_2]$ is reported in the supplementary information. Dimethyl sulfoxide (DMSO, anhydrous, ≥99%, Sigma Aldrich) was dried over 3 Å molecular sieves for 12 hr prior to use (water content = 30 ppm). Electrolyte solutions of 0.5 M, 1.0 M and 2.5 M $\text{Zn}(\text{dca})_2/\text{DMSO}$ were prepared in an Argon glovebox (Korea Kiyon with nominated levels of oxygen and water less than 1 ppm). Zinc foil (0.25 mm thick, Sigma Aldrich) were polished with sandpaper, washed with acetone, and dried under vacuum at 75 °C prior to electrochemical testing.

Electrochemistry measurements

Symmetrical cell cycling was performed to study the cell cycling ability and the Zinc metal surface state during cycling propagation. All symmetrical cell fabrication were conducted with $\text{Zn}|\text{Zn}$ 2032 coin cells (components CR2032 were purchased from Hohsen Corporation, Japan) and prepared using two Zinc metal electrodes, assembled in the glovebox. Zn foils were brushed and punched into 10 mm diameter Zn disks using a precision disk cutter. A 12 mm diameter Celgard 2400 separator was soaked with around 50 µL was sandwiched between 2 Zn metals.

Cyclic voltammetric experiments were performed on a Biologic VMP3/Z multi-channel potentiostat using a 3-electrode set-up consisting of a 1 mm diameter glassy carbon (GC) (ALS Co., Ltd, Japan) working electrode (WE) and 0.25 mm diameter Zn wire as both the counter electrode (CE) and reference electrode (RE).

Fourier transform infrared spectroscopy (FT-IR)

ATR-IR experiments were performed on a FT-IR Spectrometer (Varian 3100) with an ATR attachment (Pike, MiRacle) utilizing a diamond prism. Data was collected on Resolutions Pro software. The measurements were averaged over 64 times at a resolution of 4 cm^{-1} in the range of 600–4000 cm^{-1} . A peak between 2966–2970 cm^{-1} was used as the basis for normalization since this was the peak that changed the least with varying concentration of zinc. A background scan was performed before running each sample. All measurements were corrected by smoothing and performing ATR

corrections using the Spectrum Software, as well as the baseline correction.

Physical property measurements

The viscosity was measured using an Anton Paar AMVn for all mixtures electrolyte solutions from 25°C to 90°C. The ionic conductivity of the samples was evaluated using AC impedance spectroscopy in a frequency range of 0.1 Hz to 10 MHz using a dip cell. The measurements were performed with a frequency response analyser, Solartron 1296, driven by Solartron impedance measurement software version 3.2.0. For all mixtures, the temperature range was 25°C to 90°C. The instrument temperature was controlled by a Eurotherm 2204e thermostat. The conductivity of the electrolytes was determined by relating the touch-down point of the Nyquist plot against 0.01 M KCl/H₂O.

Thermogravimetric analysis (TGA)

TGA was undertaken on a Mettler Toledo TGA/DSC 1 STARe System. Samples were heated at 10°C/min over a temperature range of 25 to 450°C under nitrogen.

Density functional theory (DFT)

The Infrared spectroscopy was calculated on the single ion or molecule or ion pairs which were optimized first by Density Functional Theory (DFT) at B3LYP/6-311+G(d,p) level of theory in the gas phase. A scale factor of 0.9679 was applied for vibrational stretching frequencies.

Molecular dynamics (MD) simulation

Molecular dynamics was conducted on three DMSO systems with different Zn(dca)₂ concentrations of 0.5, 1.0 and 2.5 M. The force field parameters of the Zn cation and dca anion were taken from all-atom, non-polarizable CL&P force field.^[21] The force field parameters of DMSO were generated using the LigParGen online generator.^[22] The charge of DMSO was determined with the Merz-Singh-Kollman (MK) Scheme. A charge scale factor of 0.7 was adopted to reduce the total charge to account for polarisable effect. Simulation boxes were generated by randomly packing ions and molecules using packmol.^[23] Firstly, the system was relaxed at a high temperature of 498 K using a Berendsen thermostat and barostat in an *NPT* ensemble. The energy profile was generated to check whether the equilibrium is reached. Then the temperature was decreased to 298 K and the system was equilibrated again. Once an equilibrium state is reached, the further equilibration was conducted using an *NPT* ensemble with an Nöse-Hoover thermostat and a Hoover barostat, with relaxation constants of 0.5 and 10 ps, respectively. The pressure is 1 atm and the time step is 1.0 fs. The cutoffs for van der Waals force and the real space of Ewald were 12 Å. The Velocity Verlet integration algorithm was adopted. The Ewald sum method was selected, with a specified acceptable relative error of 1.0 e⁻⁵, to treat Coulomb interaction in a periodic system. All MD simulations were conducted using DL_POLY Classic

software.^[24] The densities were calculated at 298 K which fit the experimental results very well. The errors are only 0.99%, 0.83% and 0.91% for the 0.5 M, 1 M and 2.5 M Zn(dca)₂ systems, respectively.

Surface characterisation

SEM (scanning electron microscopy) and EDS (energy dispersive x-ray spectroscopy) were used to characterize the Zinc surface after cycling and determine the elemental composition. The SEM instrument (JOEL JSM IT300 Oxford) was integrated into the EDS system for element analysis.

XPS (X-ray photoelectron spectroscopy) was performed on a Thermo Scientific Nexsa spectrometer equipped with a hemispherical analyzer. The incident radiation was monochromatic Al K α X-rays (1486.6 eV) at 72 W (6 mA and 12 kV, 400×800 μm² spot). Survey (wide) and high-resolution (narrow) scans were recorded at analyzer pass energies of 150 and 50 eV, respectively. Survey scans were performed with a step size of 1.0 eV and a dwell time of 10 ms. High-resolution scans were obtained with a step size of 0.1 eV and dwell time of 50 ms. The base pressure in the analysis chamber was less than 5.0×10⁻⁹ mbar. A low-energy dual-beam (ion and electron) flood gun was used to compensate for surface charging. All data were processed using Casa XPS software and the energy calibration was referenced to the low binding energy component of the C 1s peak at 284.8 eV.

Results and Discussion

Physical properties

Table 1 summarizes the physicochemical properties of the DMSO based electrolytes in the presence of 0.5 M, 1.0 M and 2.5 M Zn(dca)₂ in the temperature range 25°C–90°C. The increase in Zn salt concentration in this work increases the density and viscosity (Figure S1a) of the electrolyte. For example, the viscosity of 0.5 M, 1.0 M and 2.5 M Zn(dca)₂/DMSO at 25°C is 3.73, 7.02 and 34.50 mPas, respectively. As an effect of high viscosity, it impedes the mobility of the ions as is generally observed in the decrease in conductivity. However, increasing the zinc salt concentration from 0.5 M (6.94 mS cm⁻¹) to 1.0 M (6.63 mS cm⁻¹) barely varies the conductivity, suggesting similar mobility of ions. Additionally, beyond 50°C, the conductivity of the 1.0 M Zn(dca)₂/DMSO electrolyte starts to exceed the conductivity of 0.5 M Zn(dca)₂/DMSO (Figure S1b) and at 90°C, the conductivity of 1.0 M Zn(dca)₂/DMSO was found to be higher (16.0 mS cm⁻¹) than that for 0.5 M Zn(dca)₂/DMSO (12.8 mS cm⁻¹). This suggests that despite having a higher content of Zn salt concentration than 0.5 M, the mobility of ions is enhanced and thus for 1.0 M Zn(dca)₂/DMSO present the highest conductivity at high temperatures.

Table 1. Density, viscosity and conductivity measurements of 0.5 M, 1.0 M and 2.5 M Zn(dca)₂/DMSO at 25 °C.

Electrolyte	Density [g mL ⁻¹] ± 0.001	Viscosity [mPas] ± 0.01	Conductivity [mS cm ⁻¹] ± 0.10
0.5 M Zn(dca) ₂ /DMSO	1.145	3.73	6.94
1.0 M Zn(dca) ₂ /DMSO	1.186	7.02	6.63
2.5 M Zn(dca) ₂ /DMSO	1.281	34.50	2.70

At 2.5 M, a significant decrease in conductivity (2.70 mS cm^{-1}) is observed at 25°C . This may imply the formation of complex species including aggregates and ion-clusters hindering ion dissociation in the electrolyte. Similar behaviour was observed by Kar et al.^[25] in their work on exploring zinc coordination in tetraglyme, in which complex zinc-chloro species were found to lower the ionicity of electrolyte at high concentrations of zinc chloride ($> 50 \text{ mol\% ZnCl}_2$). Such complex zinc species are also evident in our spectroscopic and simulation studies discussed in the section below. Interestingly enough, increasing the temperature of the 2.5 M electrolyte to 90°C , also significantly increases the conductivity one order of magnitude to 14 mS cm^{-1} making it even more ionically conductive than 0.5 M $\text{Zn}(\text{dca})_2/\text{DMSO}$. Such remarkable results observed for both the 1.0 M and 2.5 M zinc electrolytes make them suitable for high temperature zinc battery applications.

To understand the solvation environment of Zn^{2+} ions in the electrolytes under study, Fourier transform infrared spectroscopy (FT-IR) and further complemented by density functional theory (DFT) calculations were performed. Figure 1(a) shows the region of the CH_3 -wag peaks of “free” DMSO at 1052 cm^{-1} and 1024 cm^{-1} , in agreement with the literature.^[26] With increasing concentration of $\text{Zn}(\text{dca})_2$ the peak at 1052 cm^{-1} decreases in intensity while the peak at 1024 cm^{-1} increases and is red-shifted to 985 cm^{-1} . The changes of these peaks suggests that the DMSO is bound to Zn^{2+} ions upon addition of the salt. The mole ratio of each species to Zn in Table 2 also shows that with increasing concentration of $\text{Zn}(\text{dca})_2$, the mole of DMSO decreases from 28 to 6 per mole of Zn^{2+} . This suggests that in the 2.5 M $\text{Zn}(\text{dca})_2$ electrolyte, most of the DMSO is bound to Zn^{2+} ions. However, the number of DMSO molecules that are available in the 0.5 M and 1.0 M $\text{Zn}(\text{dca})_2$

systems are 28 and 14, respectively (Table 2). This implies that a large amount of DMSO will be free at these concentrations and that can play a role on the ion dynamics, such as increasing the ion mobility of Zn^{2+} ions in the electrolyte. This is further demonstrated in the higher ionic conductivity observed for 0.5 M and 1.0 M $\text{Zn}(\text{dca})_2$ systems (Tables 1 and S1b).

Figure 1(b) shows various zinc complex species arising predominantly from $[\text{dca}]^-$ in the FT-IR region $2100\text{--}2350 \text{ cm}^{-1}$. Both free and bound $\nu(\text{C}\equiv\text{N})$ peak of the $[\text{dca}]^-$ anion are observed in all three electrolytes, in the regions $2140\text{--}2110 \text{ cm}^{-1}$ and $2180\text{--}2140 \text{ cm}^{-1}$, respectively, as previously observed by Simons et al.^[27] The intensity of both bound and free $[\text{dca}]^-$ anion peaks increase with increasing concentration of $\text{Zn}(\text{dca})_2$; however, the relative intensity between the bands is different. A prominent increase in the bound region is observed at the highest concentration, 2.5 M $\text{Zn}(\text{dca})_2/\text{DMSO}$, in comparison with the free $[\text{dca}]^-$ region, as expected by the lower mol DMSO in the mixture (Table 2). The fitting of the FT-IR spectra is a useful way to understand the contributions of certain bands,^[28] and was used here to determine the exact ratio of free to bound $[\text{dca}]^-$ (Figure S2) in the region $2100\text{--}2200 \text{ cm}^{-1}$. Table S2 further indicate the ratio of bound to free $[\text{dca}]^-$ is 2, 4 and 9 for 0.5 M, 1.0 M and 2.5 M $\text{Zn}(\text{dca})_2/\text{DMSO}$ respectively, suggesting that with increasing concentration of the salt, Zn^{2+} ions are highly solvated with $[\text{dca}]^-$ anions. The broadness of the bound peak also suggests the possible presence of multiple bands that could not be easily identified within this region.

Table S3 summarises the theoretical frequency DFT calculations (in the gas phase) of all most probable Zn solvation species in this region, complementing and corroborating the experimental FT-IR. To date such use of DFT calculations to complement the FT-IR in the identification of zinc species at

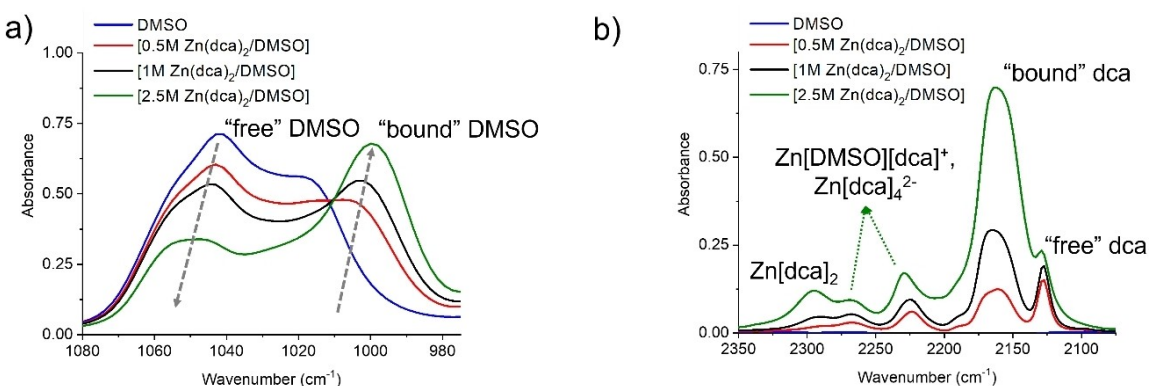


Figure 1. FT-IR spectra for electrolytes of neat DMSO and 0.5 M, 1.0 M, 2.5 M $\text{Zn}(\text{dca})_2/\text{DMSO}$ in the range from a) $2100\text{--}2200 \text{ cm}^{-1}$ and b) $980\text{--}1080 \text{ cm}^{-1}$.

Table 2. Mole ratio of Zn^{2+} , $[\text{dca}]^-$ and DMSO calculated in 0.5 M, 1.0 M and 2.5 M $\text{Zn}(\text{dca})_2/\text{DMSO}$ (25°C).

Electrolyte	Mole ratio		
	Zn	dca	DMSO
0.5 M $\text{Zn}(\text{dca})_2/\text{DMSO}$	1	2	28
1.0 M $\text{Zn}(\text{dca})_2/\text{DMSO}$	1	2	14
2.5 M $\text{Zn}(\text{dca})_2/\text{DMSO}$	1	2	6

different Zn salt concentrations has not been performed in the literature. Based on DFT simulations vibrational peaks at 2195 cm^{-1} and 2156 cm^{-1} , that can be assigned to $\text{Zn}^{2+}([\text{DMSO}]_2[\text{dca}]_2)$ and $\text{Zn}^{2+}([\text{DMSO}]_4[\text{dca}]^+)$, are present in all three electrolytes. However, these peaks are much more prominent in the presence of 2.5 M $\text{Zn}(\text{dca})_2/\text{DMSO}$. Additional peaks at approximately 2285 cm^{-1} , 2204 cm^{-1} and $2272\text{--}2282\text{ cm}^{-1}$ corresponding to [dca] rich species such as $\text{Zn}^{2+}[\text{DMSO}]_4[\text{dca}]^+$, $\text{Zn}^{2+}[\text{dca}]_4^{2-}$ and $\text{Zn}^{2+}[\text{dca}]_2$ stretching vibrations respectively are evident in both the experimental (Figure 1b) and theoretical spectra. The large number of complex zinc species, especially at the highest concentration, suggests the formation of many Zn-clusters and aggregates, which could impede the mobility of the species in solution, as observed in the viscosity and conductivity data at 25°C , as discussed earlier (Table 1).

Figure 2(a) further depicts the changes in Zn^{2+} coordination structures at different salt concentrations through calculating

radial distribution function (RDF), which represents the probability of DMSO and $[\text{dca}]^-$ anion to be in the vicinity of Zn^{2+} when the latter is located at the origin. The RDF in Figure 2(a_i) corresponds to 0.5 M $\text{Zn}(\text{dca})_2/\text{DMSO}$. Three main peaks between 2 \AA and 8 \AA are attributed to three different coordination species of Zn. At 2 \AA , in the first coordination shell, Zn is coordinated to O from DMSO and the terminal nitrogen (N1) of the $[\text{dca}]^-$ anion, i.e., $\text{Zn}-\text{N1}_{\text{dca}}$ (determined from the bond length between $\text{Zn}-\text{O}_{\text{DMSO}}$ and $\text{Zn}-\text{N1}_{\text{dca}}$). In contrast, the distance between Zn^{2+} ions and the middle nitrogen of the $[\text{dca}]^-$ anion, ($\text{Zn}-\text{N2}_{\text{dca}}$) is larger (4 \AA), implying that this nitrogen atom is not part of the first coordination shell. Figure 2(a_ii) and (a_iii) shows the RDF plots $\text{Zn}-\text{N1}_{\text{dca}}$ and $\text{Zn}-\text{O}_{\text{DMSO}}$, respectively with different Zn salt content. In general, Zn has a coordination number between 4–6.^[29] Increasing the concentration of the zinc salt from 0.5 M to 2.5 M , decreases the average CN of $\text{Zn}-\text{O}_{\text{DMSO}}$ from 5.4 to 0.7

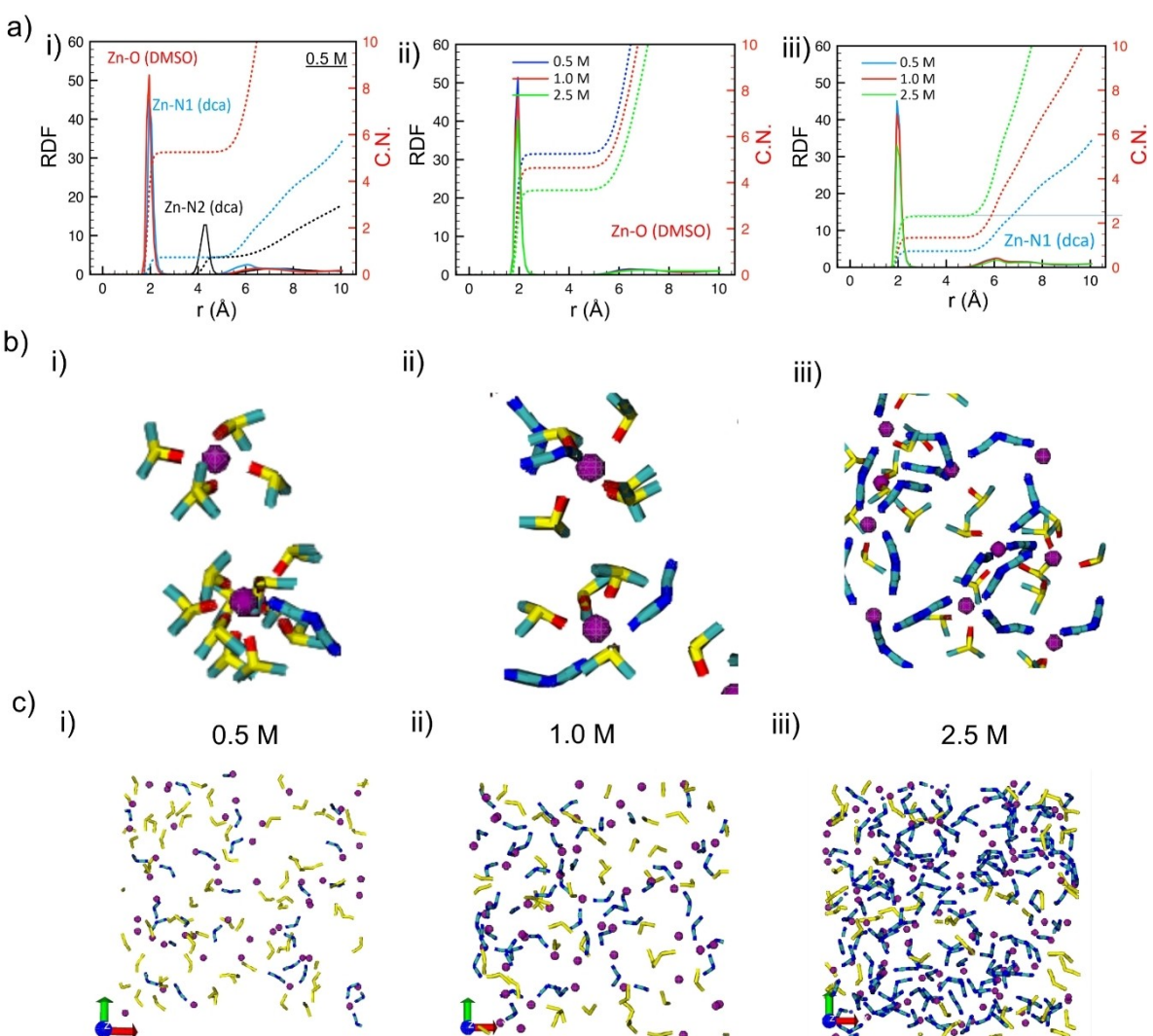


Figure 2. a) RDFs between i) Zn^{2+} and different atoms in 0.5 M $\text{Zn}(\text{dca})_2/\text{DMSO}$ and ii) $\text{Zn}-\text{O1}_{\text{DMSO}}$ iii) $\text{Zn}-\text{N1}_{\text{dca}}$ for 0.5 M , 1.0 M and 2.5 M $\text{Zn}(\text{dca})_2/\text{DMSO}$; b) snapshots of the Zn^{2+} ion coordination environment in DMSO and $[\text{dca}]^-$ with i) 0.5 M $\text{Zn}(\text{dca})_2/\text{DMSO}$, ii) 1.0 M $\text{Zn}(\text{dca})_2/\text{DMSO}$ and iii) 2.5 M $\text{Zn}(\text{dca})_2/\text{DMSO}$ (purple = zinc, dark blue = nitrogen, yellow = sulfur, light blue = carbon, red = oxygen); c) snapshots depicting free $[\text{dca}]^-$ and coordinated $[\text{dca}]^-$ with Zn^{2+} ions in i) 0.5 M $\text{Zn}(\text{dca})_2/\text{DMSO}$, ii) 1.0 M $\text{Zn}(\text{dca})_2/\text{DMSO}$ and iii) 2.5 M $\text{Zn}(\text{dca})_2/\text{DMSO}$ (purple = zinc, blue = coordinated $[\text{dca}]^-$, yellow = uncoordinated $[\text{dca}]^-$).

(Figure 2a_ii) and increases the CN of Zn–N1_{dca} from almost 0.7 to 2.4 (Figure 2a_iii), resulting in Zn average coordination number of 6 for all three systems. Moreover, with increasing concentration of zinc salt, the [dca]⁻ anion coordination to Zn changes from monodentate to bridging as further discussed in the following section.

The snapshots in Figure 2(b and c) provide a more detailed understanding of the Zn²⁺ ion coordination environment at different salt concentrations, further complementing the RDF plots. At the lowest salt concentration, the snapshots in Figure 2(b_i) show that Zn²⁺ ions are largely solvated by DMSO while the [dca]⁻ anions remain mostly uncoordinated in the electrolyte (Figure 2c_i). Figure 2(c_i) further demonstrates that only a small fraction of the anions coordinates to Zn²⁺ ions, in a monodentate manner (through N1). In contrast, at 1.0 M Zn(dca)₂/DMSO (Figure 2b_ii and c_ii) DMSO molecules and most of [dca]⁻ anions are coordinated to Zn²⁺ ions providing mixed ligand species. The snapshots also show that the [dca]⁻ anions act as both monodentate and bridging ligands between Zn²⁺ ions, as also observed previously by Simons et al.^[27] Evidently at 2.5 M Zn(dca)₂/DMSO (Figure 2b_iii and c_iii), along with DMSO, the majority of [dca]⁻ anions are coordinated to Zn²⁺ ions, as also highlighted in the RDF plot in Figure 2aiii in which the CN of Zn–N1_{dca} is the highest at 2.4. Furthermore, the [dca]⁻ anions are mainly acting as bridging ligands to Zn²⁺ ions.

Overall, although the high CN of Zn–O_{DMSO} in all three electrolytes imply that Zn prefers to solvate to the oxygen

atoms of the strongly coordinating DMSO molecules, the decrease in CN of Zn–O_{DMSO} and the increase in CN of Zn–N1_{dca} also suggests that with increasing concentration of Zn(dca)₂, the [dca]⁻ anion competes with DMSO molecules and begin to dominate the solvation of Zn²⁺ ions, providing mixed ligand structures in both the 1.0 M and 2.5 M electrolytes. This further corroborates the experimental and simulations FT-IR results, in which a larger ratio of bound dca is specifically observed in 2.5 M Zn(dca)₂/DMSO, with multiple bands observed in the region 2285–2275 cm⁻¹, providing an overall [dca]-rich environment for this electrolyte.

Electrochemical properties

Figure 3(a and b) compares the cyclic voltammogram (CV) of Zn(dca)₂/DMSO of the three different Zn(dca)₂ based electrolyte mixtures on glassy carbon (GC) at cycle 1 and cycle 5, respectively. CVs are an informative tool to understand the metal deposition and the diffusion of metal ions with varying salt concentration.^[30] In all three electrolytes, one reduction and one oxidation process are observed, corresponding to the plating and stripping of Zn metal on the working electrode. For clarity, the electrochemical window of DMSO is provided in Figure S3, in which no reductive and oxidative peaks were observed within the electrochemical potential window of interest, -1.9 V to +2.4 V vs. Zn. In the first cycle corresponding to 0.5 M Zn(dca)₂/DMSO (Figure 3a), the onset of the

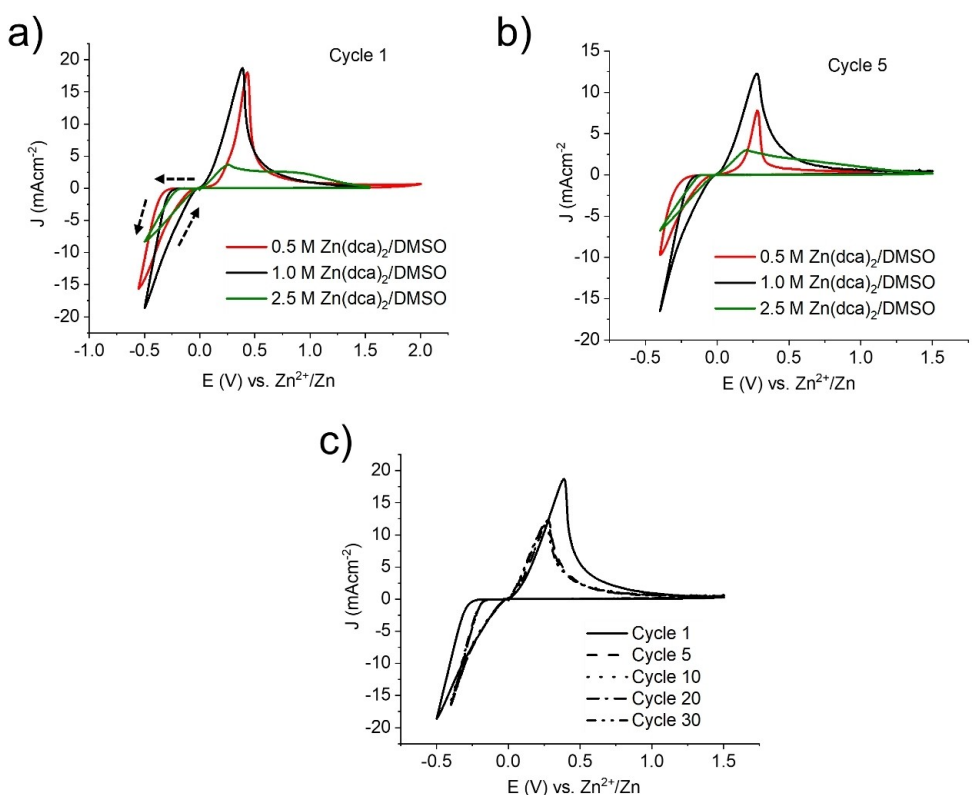


Figure 3. Cyclic voltammetry (CV) of 0.5, 1.0 and 2.5 M Zn(dca)₂/DMSO at a) Cycle 1 and b) Cycle 5; c) CV of 1.0 M Zn(dca)₂/DMSO over 30 cycles at room temperature under Argon. (Working electrode: GC, Scan rate : 25 mV/s)

reduction of Zn^{2+} ions ($Zn^{2+} + 2e^- \rightarrow Zn$) occurs at -0.30 V vs. Zn. However, with increasing concentration of the zinc salt, a more positive shift in the reduction potential for the 1.0 M $Zn(dca)_2/DMSO$ ($E_{onset} = -0.25$ V vs. Zn^{2+}/Zn) and 2.5 M $Zn(dca)_2/DMSO$ ($E_{onset} = -0.23$ V vs. Zn^{2+}/Zn) electrolyte is observed suggesting that reduction of zinc is facilitated in these electrolytes. This can be attributed to the large amount of Zn^{2+} ions available at higher concentrations to reduce at the interface; however, changes in the speciation and mixed ligands can facilitate the reduction process. For instance, in comparison to the 0.5 M Zn electrolyte which is exclusively dominated by Zn-DMSO coordination, a large amount of weaker coordinating $[dca]^-$ anions is present in the 1.0 M and 2.5 M electrolytes. This can enable the Zn complex species in these electrolytes to dissociate more easily, resulting in a more positive shift in the reduction potential.^[31] Additionally, in comparison to the 0.5 M electrolyte in which the dca is coordinated to Zn in a monodentate manner, the presence of bridging $[dca]$ in the Zn-dca coordination for 1.0 and 2.5 M electrolyte, can also result in the formation of a weaker ligand.

In cycle 1 (Figure 3a), the peak oxidative currents of Zn barely increase from 17 to 18 mA cm⁻² when the concentration is increased from 0.5 M to 1.0 M, but significantly decrease to 3.0 mA cm⁻² when the concentration of $Zn(dca)_2$ is further increased to 2.5 M. Similarly, the reductive currents of Zn increase from -16 to -18 mA cm⁻² when the concentration is increased from 0.5 to 1.0 M but decrease to -7.0 mA cm⁻² when the concentration of $Zn(dca)_2$ is further increased to 2.5 M. The results here are also consistent with the ionic conductivities of the electrolytes (Table 1 and Figure S2) in which similar high conductivities were observed for the 0.5 M and 1.0 M electrolyte (6.94 and 6.63 mS cm⁻¹ respectively at 25 °C), while a lower conductivity was observed for the 2.5 M electrolyte (6.63 mS cm⁻¹). Aside from the main anodic peak at $+0.25$ V (vs. Zn^{2+}/Zn), a broad second anodic peak close to $+1$ V (vs. Zn^{2+}/Zn) appears to be prominent for the latter electrolyte. This can be postulated to the various zinc species present, as observed in the FT-IR and MD simulations. However, further studies are required to understand this phenomenon.

While the changes in both the cathodic and anodic current densities of the 2.5 and 1.0 M electrolytes remain insignificant in cycle 5 (Figure 3b), a large drop in current density (-10 and 7 mA cm⁻²) is observed for both the reductive and oxidative processes in the 0.5 M electrolyte respectively. This is likely to be due to the formation of a passivating film on the working electrode upon cycling can impede the electrochemical performance of Zn.

Considering the Zn speciation described before, it may indicate that, unlike the coordination behaviour in 0.5 M $Zn(dca)_2/DMSO$ in which Zn^{2+} ions exclusively coordinate to DMSO molecules, the coordination of Zn^{2+} ions with some of both DMSO molecules and $[dca]$ molecules is required to form stable species and undergo favourable electrochemistry, as is observed for 1.0 M $Zn(dca)_2/DMSO$. In fact, Figure 3(c) illustrates stable cycling of Zn^{2+}/Zn over 30 cycles with insignificant change to the cathodic and anodic processes for this electrolyte. Overall, the 1.0 M $Zn(dca)_2/DMSO$ electrolyte showed low

overpotentials (peak to peak potential, $\Delta E_p = 0.018$ V) and highest cathodic and anodic current densities (16 and 11 mA cm⁻², respectively).

Zinc symmetric cells

The compatibility of zinc electrolytes with Zn anode was initially tested using zinc symmetric cells. Due to the viscosity of the electrolytes, the cells were rested for 24 h prior to undergoing zinc cycling at 1.0 mA cm⁻² (0.5 mAh cm⁻²) to ensure complete wetting of the separator with the electrolyte. Furthermore, the SEM images in Figure S4 shows that in comparison to pristine zinc anode (Figure S4a), the formation of a passivating layer on the zinc anode occurs after resting the cell for 24 h (Figure S4b) in the presence of 1.0 M $Zn(dca)_2/DMSO$. The impedance in Figure S4c also decreases upon resting suggesting the formation of a stable and conductive SEI on the electrode. Such resting protocols have been previously implemented by many researchers, particularly in the lithium and sodium battery field, to obtain a uniform and improved SEI on the anode for stable metal cycling.^[32] Consequently, in comparison to the none-resting cell, the Zn|Zn symmetric cell upon resting for 24 h overall demonstrated significantly lower overpotentials over 100 cycles at 1 mA cm⁻² (0.5 mAh cm⁻²) (Figure S4d). Henceforth, all cells were prepared and rested for 24 h prior to cycling.

Figure 4 displays the symmetric cycling of Zn in the presence of 0.5 M, 1.0 M and 2.5 M $Zn(dca)_2/DMSO$ over 90 cycles, and selected cycles (Cycle 1, 10, 50 and 90) at 1.0 mA cm⁻² (0.5 mAh cm⁻²). All cells were rested for 24 h followed by 30 minutes charge and discharge. Further electrochemical impedance spectroscopy (EIS) (Figure S5) indicates the overall interfacial resistance of all three electrolytes before and after cycling. An example of a fitted impedance spectrum gained from Zn|Zn symmetrical cell containing 1.0 M $Zn(dca)_2/DMSO$ after 90 cycles is demonstrated in Figure S5(a). The best fits were achieved when employing a two-component layer model showing two semi-circles, i.e., R_{int} and R_{ct} , where R_{int} represents the bulk resistance of the zinc interphase layer and R_{ct} represents the charge transfer of zinc ions through the interphase.^[33]

Prior to cycling, all three electrolytes show high interfacial resistance (> 1000 ohms). However, the resistance decreases significantly upon cycling. In the presence of 0.5 M $Zn(dca)_2/DMSO$, low overpotentials are observed in the first 50 cycles (0.12 V) and the overall interfacial resistance also decreases to almost 140 ohms (Figure S5b_i). However soon after, the cycling behaviour of zinc becomes erratic with some voltage spiking evident after 70 cycles. Overpotentials as high 0.3 V (vs. Zn^{2+}/Zn) is observed towards the end of cell of the 90 cycles and resistance is increased again (> 200 ohm). Further scanning electron microscopy (SEM) images in Figure 4(b) show that in comparison to the pristine zinc foil uneven distribution of loose zinc deposits is formed on the zinc anode. In contrast, although high overpotentials (0.17 V) was observed for 1.0 M $Zn(dca)_2/DMSO$ initially in the first 20 cycles, the overpotentials soon

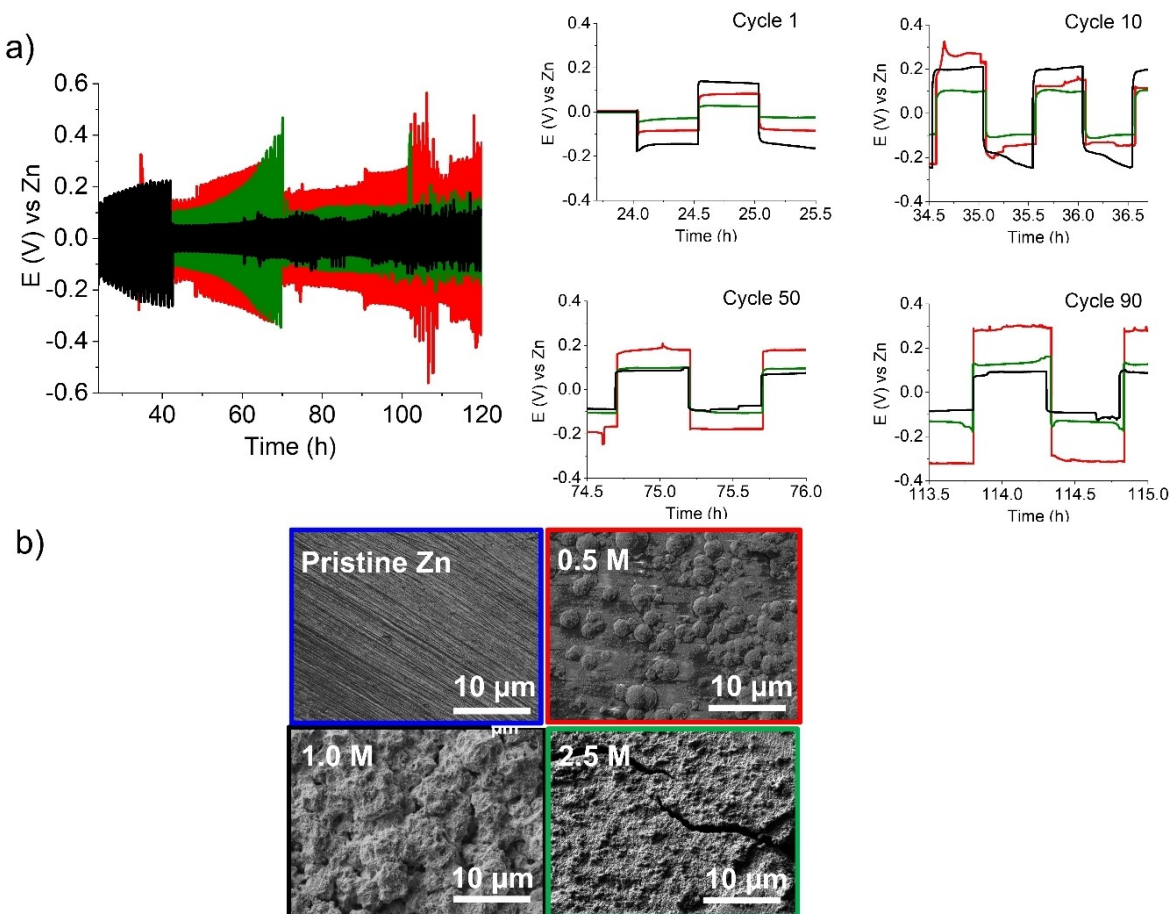


Figure 4. a) Galvanostatic charge/discharge profile of Zn/Zn symmetrical cells in the presence of 0.5 M (red), 1.0 M (black) and 2.5 M Zn(dca)₂/DMSO (green) at 1.0 mA cm⁻² 120 h (0.5 mAh cm⁻²). Inset shows charge/discharge profiles at Cycles 1, 10, 50 and 90; b) SEM images of zinc electrode post-cycling of the electrolytes.

decreases after this cycle showing stable cycling over the next 70 cycles with the lowest overpotentials (0.05 V). EIS data in Figure S5(b_ii) also suggests that the interfacial resistance remains low and unchanged upon further cycling (20 ohms). This indicates that the SEI layer is more conductive and favouring further zinc deposition/stripping. SEM image in Figure 4(b) also demonstrates a more compact and homogeneous, non-dendritic morphology. The overpotentials observed in the charge/discharge cycles are much lower than those reported by many authors in Zn|Zn symmetric cycling in various organic electrolytes and under similar conditions.^[12a,d,34] For instance, in their work on Zn|Zn symmetric cycling in the presence of Kao-ian 0.25 M Zn(OTf)₂/DMSO at the same applied current 1.0 mA cm⁻² (1.0 mAh cm⁻²), an average overpotential of 0.001 V was reported over 50 cycles.^[12a] Therefore, these results suggest that the presence of [dca]⁻ anions play a key role in enabling long term zinc cycling. At 2.5 M, a gradual increase in overpotential is observed at which the maximum overpotential of 0.34 V (vs. Zn²⁺/Zn) reached at the 48th cycle. Following this, a drop in overpotential, to 0.1 V and a decrease in interfacial resistance (Figure S5b_iii) is observed for the rest of the cycling. A thick layer of zinc deposit in the 2.5 M system is evident in the SEM image. Some cracks are also visible on the

surface, suggesting that the deposition of zinc is non-uniform. Overall, the low overpotentials, low interfacial resistance, uniform zinc morphology and stable charge/discharge cycling of zinc in the presence of 1.0 M Zn(dca)₂/DMSO at 1.0 mA cm⁻² makes this electrolyte a highly promising candidate for rechargeable zinc batteries.

Figure 5 illustrates the XPS high resolution Zn 2p spectra of the zinc electrode after 90 cycles on the zinc surface and at different depth. Figure 5(a) shows two peaks for the uncycled Zn electrode at 1021.3 and 1045.0 eV corresponding to metallic Zn 2p_{3/2} and 2p_{1/2} respectively with a characteristic peak separation of 23.0 eV.^[34b,35] Interestingly enough, when the Zn|Zn symmetric cells are cycled in 0.5 M Zn(dca)₂/DMSO, the main Zn 2p_{3/2} peak for Zn metal remained barely unchanged at 1021.5 eV while two additional smaller Zn²⁺ peaks corresponding to Zn(OH)₂^[36] and interstitial zinc (Zn₃S)^[37] at 1023.3 and 1024.8 eV respectively arises. The former band was also observed by Dilasari and co-workers^[38] that was attributed to the oxidation of Zn on the surface to Zn(OH)₂ in the presence of a hydrated ionic liquid. A shift of the Zn 2p_{3/2} peak to a higher binding energy (BE) is also evident on the zinc surface of the cells cycled in the presence of 1.0 and 2.5 M Zn(dca)₂/DMSO electrolytes. For instance, the Zn 2p_{3/2} peak was

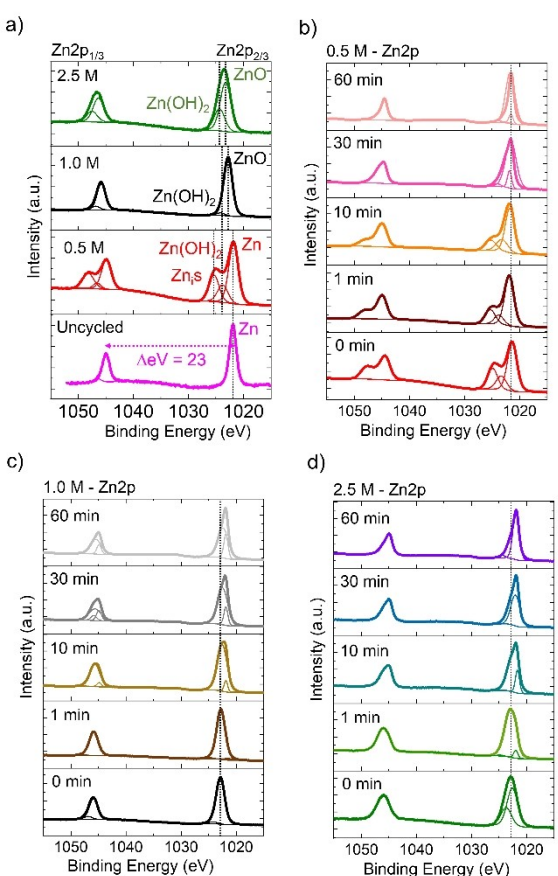


Figure 5. a) High resolution Zn 2p XPS spectra of cycled Zn anodes (90 cycles, 1 mA cm^{-2}) at 0.5 M (red), 1.0 M (black), 2.5 M (green) Zn(dca)₂/DMSO and uncycled Zn electrode (pink) (immersed in DMSO for 24 h); etching depth Zn 2p profile of the cycled zinc surface showing in b) 0.5 M Zn(dca)₂/DMSO, c) 1.0 M Zn(dca)₂/DMSO and d) 2.5 M Zn(dca)₂/DMSO.

observed at 1022.8 eV and 1023.25 eV for 1.0 and 2.5 M Zn(dca)₂/DMSO, respectively. These peaks are attributed to ZnO and also suggest a change from metallic Zn to Zn²⁺ as the salt concentration in the electrolyte increases.^[38] An additional smaller peak at higher binding energy at 1023.2 and 1023.8 eV is also observed in both the electrolytes, corresponding to Zn(OH)₂.^[36]

Figure 5(b) shows that the binding energy of the main Zn metal peak at 1021.5 eV remains largely unchanged with etching for the 0.5 M electrolyte. An insignificant decrease in atomic% (at.%) after 60 min of Ar⁺ sputtering for this peak is also observed, 57 at.% at 0 min vs. 53 at.% at 60 min. In contrast, the intensity of both the Zn₃S and Zn(OH)₂ component peaks decrease from 25 at.% and 18 at.% at 0 min to 3.0 at.% and 10 at.%, respectively at 60 min, suggesting Zn₃S and Zn(OH)₂ species accounting for the outer layer of the SEI. The presence of metallic Zn in the inner layer of the zinc electrode is observed in both the 1.0 M (Figure 5c) and 2.5 M (Figure 5d) systems. However, the Zn metallic peak begins to appear after 10 min of Ar⁺ sputtering in the 1.0 M system while it appears earlier at 1 min of Ar⁺ sputtering in the 2.5 M system. This phenomenon suggests that the inner SEI layer is mostly dominated by metallic Zn in both the 0.5 M and 2.5 M Zn(dca)₂/DMSO electrolyte while a mixture of oxidized and metallic Zn governs the SEI layer in the 1.0 M Zn(dca)₂/DMSO electrolyte. This may play a key role in the stable electrochemical cycling of Zn observed in Figure 4 for this electrolyte.

Figure 6(a-c) demonstrates the C 1s, O 1s and N 1s spectra of the zinc surface after the electrochemical cycling of zinc in 0.5 M, 1.0 M and 2.5 M Zn(dca)₂/DMSO over 90 cycles. It must be noted that while the S 2p XPS experiment was performed, the signal was very low with low atomic percent of sulfur detected (<2 at.%) in all three systems (Table S4) suggesting that the breakdown products at the zinc interface are mainly attributed to the [dca]⁻ anion and not the organic solvent

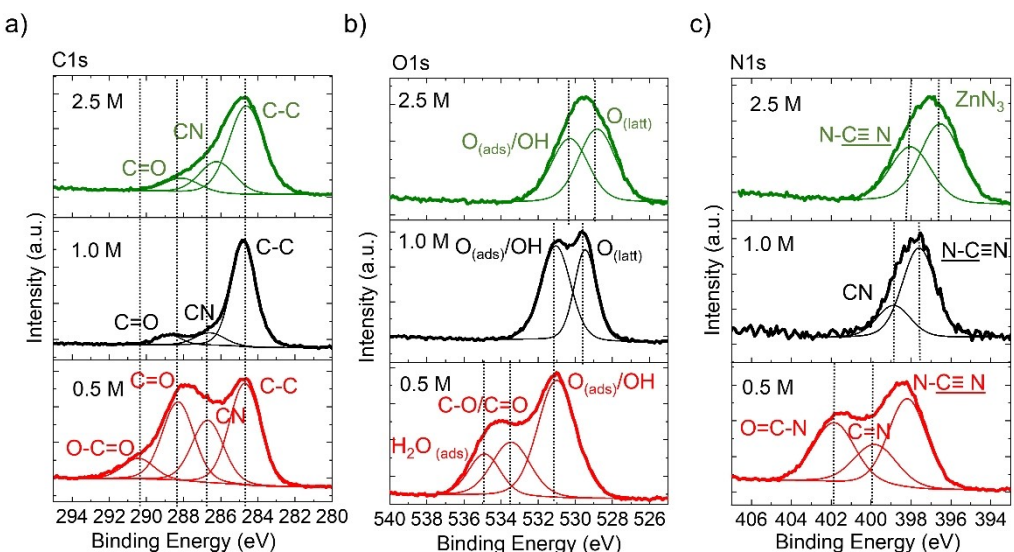


Figure 6. High resolution a) C 1s, b) O 1s and c) N 1s XPS spectra of cycled Zn anodes (90 cycles, 1 mA cm^{-2}) at 0.5 M (red), 1.0 M (black), 2.5 M (green) Zn(dca)₂/DMSO.

DMSO, where S is present. In comparison to the 1.0 and 2.5 M electrolytes, multiple peaks are observed on the zinc surface in the presence of 0.5 M Zn(dca)₂/DMSO for the different elements. For example, the C 1s spectra (Figure 6a) of the zinc surface when cycled in the 1.0 and 2.5 M electrolytes show the existence of ketones (C=O), cyano-containing species (CN) and elemental C (C–C) at 288.3, 286.7 and 284.7 eV, respectively.^[39] The at.% of each of the three species were found to be similar in both electrolytes. For example, the at.% of C=O, CN and C–C are 8%, 11% and 81% in the 1.0 M electrolyte and 10%, 14% and 66% in the 2.5 M electrolyte. In contrast, the at.% of the three species in the 0.5 M electrolyte was found to be significantly higher for C=O and CN (30% and 24%) but lower for C–C (39%). Moreover, an additional carbonate (CO₃)²⁻ peak (at.% = 8%) is also observed at 290.4 eV, suggesting an overall higher content of organic-rich SEI layer formed from this electrolyte.

Furthermore, O 1s spectra in Figure 6(b) show the presence of adsorbed oxygen (O_(ads)),^[40] organic C–O/C=O^[41] and adsorbed water (H₂O_(ads))^[42] at 530.9 eV (at.% = 57%), 533.4 eV (at.% = 26%) and 534.9 eV (at.% = 17%), respectively for this electrolyte. The latter contaminant is often known to be detrimental in the electrochemical cycling of metals^[12d,43] and may explain the poor charge/discharge cycling of zinc in 0.5 M Zn(dca)₂/DMSO together with the organic residues explained above, as observed in Figure 4(a). In contrast, no H₂O_(ads) peak and fewer organic/inorganic-rich species was observed in the N 1s and O 1s spectra for the 1.0 and 2.5 M system. For instance, the O 1s spectra shows only two bands in the 1.0 M electrolyte corresponding to 529.5 eV (at.% = 42%) and 531.1 eV (at.% = 58%). Similar bands were observed by Yang et al.^[44] and others^[45] who described the band at 529.5 eV to fall within the region of

lattice oxygen (O_{latt}), 528–530 eV. Although the additional band at 531.1 eV falls within the region of surface adsorbed oxygen (O_{ads})^[40] between 531–532 eV and can be ascribed to Zn–O bonding in ZnO, it can also be attributed to Zn–OH peak as also observed by Al-Gaashani et al.^[46] Thus, since both ZnO and Zn(OH)₂ peaks are also observed in the Zn 2p spectra as discussed earlier, it is most likely that both O_{ads} and OH species are present in this region. These species were also observed in the 2.5 M electrolyte where the O_{latt} peak is observed at 528.8 eV (at.% = 54%) and the O_{ads}/OH peak is observed at 530.3 eV (at.% = 47%).

The N 1s spectra in Figure 6(c) shows peaks corresponding to amide (N–C=O),^[47] cyano and nitrile-containing species CN^[48] and NC≡N^[49] at 398.2 eV (at.% = 45%), 399.8 eV (at.% = 23%) and 401.0 eV (at.% = 32.3%), respectively for the 0.5 M electrolyte. In comparison, the N 1s spectra of 1.0 and 2.5 M electrolyte show similar behavior on both the surface and the inner layer of the zinc electrode. For instance, unlike in the case of 0.5 M, amide is not observed in the presence of the higher concentrated electrolytes (1.0 and 2.5 M), while nitrile groups are observed on the zinc surface in both systems. At 1.0 M, the presence of NC≡N (at.% = 74%, 397.6 eV) and CN (at.% = 26%, 398.9 eV) is observed on the zinc surface, while NC≡N (at.% = 41%, 398.0 eV) and zinc nitride (Zn₃N₂)^[50] (at.% = 59%, 396.5 eV) were observed in the case of the 2.5 M electrolyte. Nevertheless, Figure 7 shows that while Zn₃N₂ is not evident in the presence of 0.5 M electrolyte (Figure 7a), it is clearly observed with etching in the 1.0 M electrolyte (Figure 7b) and also remains in the inner layer of the zinc surface when the cell is cycled in both the 1.0 and the 2.5 M electrolyte (Figure 7c). Although the at.% of Zn₃N₂ is lower in the 1.0 M electrolyte (40%) when compared to the 2.5 M electrolyte (60%) after

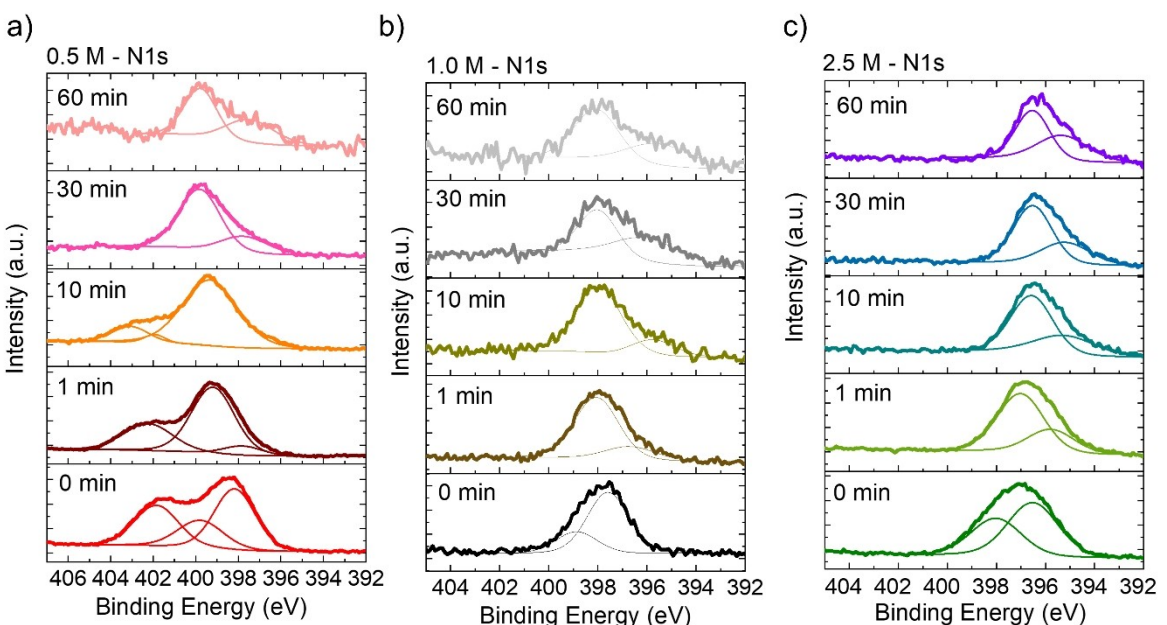


Figure 7. Etching depth profile of the cycled zinc surface (90 cycles, 1 mA cm⁻²) showing the N 1s XPS spectra in a) 0.5 M Zn(dca)₂/DMSO, b) 1.0 M Zn(dca)₂/DMSO and c) 2.5 M Zn(dca)₂/DMSO.

60 min of Ar^+ sputtering, the overall at.% of these species in both systems is still significant. Furthermore, it suggests that the large amount of [dca] molecules available in such highly concentrated electrolytes ($>1.0 \text{ M}$) may cause some of the anion to decompose and form a stable, conductive nitride-rich SEI layer, as observed in the stable electrochemical cycling of Zn in the two electrolytes. Therefore, this implies that $[\text{dca}]^-$ anions, especially at $\geq 1.0 \text{ M}$ plays a beneficial in forming a stable SEI layer and supporting the electrochemical cycling of zinc and should be considered as a highly promising electrolyte for rechargeable zinc batteries.

Conclusion

In this work, a new organic, non-fluorinated, low-cost zinc electrolytes composed of $\text{Zn}(\text{dca})_2$ in DMSO was shown to support the electrochemical cycling of zinc over 90 cycles. Both FT-IR and MD simulation studies illustrate that with increasing concentration of $\text{Zn}(\text{dca})_2$, the coordination number of $\text{Zn}-\text{O}_{\text{DMSO}}$ decreases while $\text{Zn}-\text{N}1_{\text{dca}}$ starts to increase suggesting that the $[\text{dca}]^-$ anion competes with DMSO molecules and begin to dominate the solvation of Zn^{2+} ions. Thus, the solvation sphere of Zn changes from a highly dominated Zn-DMSO coordination to a mixed ligand coordination in which Zn coordinates to both DMSO and $[\text{dca}]^-$ anions. Such mixed ligand species is providing facile electrochemical reduction of Zn as observed in the 1.0 M and 2.5 M $\text{Zn}(\text{dca})_2/\text{DMSO}$ in which a more positive onset reduction potential (-0.25 and -0.23 V vs. Zn^{2+}/Zn respectively) was observed in comparison to 0.5 M $\text{Zn}(\text{dca})_2/\text{DMSO}$ (-0.30 V vs. Zn^{2+}/Zn). Further post-mortem XPS analysis reveal that at lower concentrations [0.5 M $\text{Zn}(\text{dca})_2$], many unwanted decomposition products such as elemental C-C, carbonates and water are generated on both the surface and the inner layer of the zinc electrode, resulting in poor electrochemical cycling of Zn. In contrast, the formation of inorganic rich species such as Zn_3N_2 helps form a stable SEI layer in the presence of 1.0 and 2.5 M $\text{Zn}(\text{dca})_2/\text{DMSO}$. Additionally in the 1.0 M electrolyte, a mixture of both oxidised and metallic zinc is observed with etching depth profile. Thus, it is postulated that these species play a key role in forming a stable SEI at the zinc anode interface as well as supporting the electrochemical reversibility of zinc over 90 cycles at 1.0 mA cm^{-2} with low overpotentials (0.05 V). This work opens the pathway to explore these electrolytes, particularly at high [dca] concentrations ($\geq 1.0 \text{ M}$) in the long-term cycling of zinc in rechargeable zinc batteries, including zinc-ion and zinc-air, and will be the focus of our future work.

Acknowledgements

The authors acknowledge the Australian Research Council (ARC) Centre for Training Centre for Future Energy Storage Technologies (storEnergy) (IC180100049) for their funding. M.K. further acknowledges the Alfred Deakin Postdoctoral Fellowship (ADPRF) for funding. The authors also acknowledge use of the facilities

and the assistance of Yvonne Hora at the Monash X-ray Platform. M.K. acknowledges the Alfred Deakin Postdoctoral Research Fellowship (ADPRF) for funding. F.C. acknowledges the Australian Research Council (ARC) for funding via the Australian Centre for Electromaterials Science, grant CE140100012 and the computational resources provided by the Australian Government through National Computational Infrastructure (NCI) under the National Computational Merit Allocation Scheme (NCMAS). Open Access publishing facilitated by Deakin University, as part of the Wiley - Deakin University agreement via the Council of Australian University Librarians.

Conflict of Interest

The authors declare no conflict of interest.

Data Availability Statement

The data that support the findings of this study are available from the corresponding author upon reasonable request.

Keywords: batteries • electrochemistry • organic electrolytes • non-fluorinated • non-aqueous • simulation • zinc batteries • $\text{Zn}(\text{dca})_2$

- [1] a) J. Yang, B. Yin, Y. Sun, H. Pan, W. Sun, B. Jia, S. Zhang, T. Ma, *Nano-Micro Lett.* **2022**, *14*, 42; b) Z. Xing, C. Huang, Z. Hu, *Coord. Chem. Rev.* **2022**, *452*, 214299; c) H. Yan, X. Zhang, Z. Yang, M. Xia, C. Xu, Y. Liu, H. Yu, L. Zhang, J. Shu, *Coord. Chem. Rev.* **2022**, *452*, 214297.
- [2] M. B. Lim, T. N. Lambert, B. R. Chalamala, *Mater. Sci. Eng. R* **2021**, *143*, 100593.
- [3] a) Z. Zeng, Y. Zeng, L. Sun, H. Mi, L. Deng, P. Zhang, X. Ren, Y. Li, *Nanoscale* **2021**, *13*, 12223–12232; b) Y. Gui, Y. Lei, B. A. Fan, *Front. Chem.* **2020**, *8*.
- [4] G. Fang, J. Zhou, A. Pan, S. Liang, *ACS Energy Lett.* **2018**, *3*, 2480–2501.
- [5] a) C. Zhang, W. Shin, L. Zhu, C. Chen, J. C. Neuefeind, Y. Xu, S. I. Allec, C. Liu, Z. Wei, A. Daniyar, J.-X. Jiang, C. Fang, P. Alex Greaney, X. Ji, *Carbon Energy* **2021**, *3*, 339–348; b) Q. Zhang, Y. Ma, Y. Lu, X. Zhou, L. Lin, L. Li, Z. Yan, Q. Zhao, K. Zhang, J. Chen, *Angew. Chem. Int. Ed.* **2021**, *60*, 23357–23364; c) Y. Zhang, G. Wan, N. H. C. Lewis, J. Mars, S. E. Bone, H.-G. Steinrück, M. R. Lukatskaya, N. J. Weadock, M. Bajdich, O. Borodin, A. Tokmakoff, M. F. Toney, E. J. Maginn, *ACS Energy Lett.* **2021**, *6*, 3458–3463; d) F. Wang, O. Borodin, T. Gao, X. Fan, W. Sun, F. Han, A. Faraone, J. A. Dura, K. Xu, C. Wang, *Nat. Mater.* **2018**, *17*, 543–549.
- [6] T. F. Burton, R. Jommongkol, Y. Zhu, S. Deebansok, K. Chitbankluai, J. Deng, O. Fontaine, *Curr. Opin. Electrochem.* **2022**, *35*, 101070.
- [7] Y. Chen, S. Guo, L. Qin, Q. Wan, Y. Pan, M. Zhou, M. Long, G. Fang, S. Liang, *Batteries & Supercaps* **2022**, *5*, e202200001.
- [8] S. Guo, L. Qin, C. Hu, L. Li, Z. Luo, G. Fang, S. Liang, *Adv. Energy Mater.* **2012**, 2200730.
- [9] A. Naveed, T. Rasheed, B. Raza, J. Chen, J. Yang, N. Yanna, J. Wang, *Energy Storage Mater.* **2022**, *44*, 206–230.
- [10] S.-D. Han, N. N. Rajput, X. Qu, B. Pan, M. He, M. S. Ferrandon, C. Liao, K. A. Persson, A. K. Burrell, *ACS Appl. Mater. Interfaces* **2016**, *8*, 3021–3031.
- [11] D. Han, C. Cui, K. Zhang, Z. Wang, J. Gao, Y. Guo, Z. Zhang, S. Wu, L. Yin, Z. Weng, F. Kang, Q.-H. Yang, *Nat. Sustain.* **2022**, *5*, 205–213.
- [12] a) W. Kao-ian, M. T. Nguyen, T. Yonezawa, R. Pornprasertsuk, J. Qin, S. Siwamogsatham, S. Kheawhom, *Mater. Today Energ.* **2021**, *21*, 100738; b) A. S. Etman, M. Carboni, J. Sun, R. Younesi, *Energ. Tech.* **2020**, *8*, 2000358; c) X. Qiu, N. Wang, X. Dong, J. Xu, K. Zhou, W. Li, Y. Wang, *Angew. Chem. Int. Ed.* **2021**, *60*, 21025–21032; d) A. Naveed, H. Yang, J. Yang, Y. Nuli, J. Wang, *Angew. Chem. Int. Ed.* **2019**, *58*, 2760–2764;

- Angew. Chem.* **2019**, *131*, 2786–2790; e) Y. Dong, S. Di, F. Zhang, X. Bian, Y. Wang, J. Xu, L. Wang, F. Cheng, N. Zhang, *J. Mater. Chem. A* **2020**, *8*, 3252–3261.
- [13] a) N. Zhang, Y. Dong, Y. Wang, Y. Wang, J. Li, J. Xu, Y. Liu, L. Jiao, F. Cheng, *ACS Appl. Mater. Interfaces* **2019**, *11*, 32978–32986; b) Z. Chen, Y. Tang, X. Du, B. Chen, G. Lu, X. Han, Y. Zhang, W. Yang, P. Han, J. Zhao, G. Cui, *Angew. Chem. Int. Ed.* **2020**, *59*, 21769–21777; *Angew. Chem.* **2020**, *132*, 21953–21961.
- [14] A. Naveed, H. Yang, Y. Shao, J. Yang, N. Yanna, J. Liu, S. Shi, L. Zhang, A. Ye, B. He, J. Wang, *Adv. Mater.* **2019**, *31*, 1900668.
- [15] N. Wang, X. Dong, B. Wang, Z. Guo, Z. Wang, R. Wang, X. Qiu, Y. Wang, *Angew. Chem. Int. Ed.* **2020**, *59*, 14577–14583; *Angew. Chem.* **2020**, *132*, 14685–14691.
- [16] B. Raza, A. Naveed, J. chen, H. Lu, T. Rasheed, J. Yang, Y. NuLi, J. Wang, *Energy Storage Mater.* **2022**, *46*, 523–534.
- [17] a) D. Feng, F. Cao, L. Hou, T. Li, Y. Jiao, P. Wu, *Small* **2021**, *17*, 2103195; b) Y. Geng, L. Pan, Z. Peng, Z. Sun, H. Lin, C. Mao, L. Wang, L. Dai, H. Liu, K. Pan, X. Wu, Q. Zhang, Z. He, *Energy Storage Mater.* **2022**, *51*, 733–755.
- [18] a) T. J. Simons, M. Salsamendi, P. C. Howlett, M. Forsyth, D. R. MacFarlane, *ChemElectroChem* **2014**, *1*, 1688–1697; b) T. J. Simons, D. R. MacFarlane, M. Forsyth, P. C. Howlett, C. Pozo-Gonzalo, *ChemElectroChem* **2015**, *2*, 2071–2078.
- [19] M. Forsyth, H. Yoon, F. Chen, H. Zhu, D. R. MacFarlane, M. Armand, P. C. Howlett, *J. Phys. Chem. C* **2016**, *120*, 4276–4286.
- [20] H. Qiu, X. Du, J. Zhao, Y. Wang, J. Ju, Z. Chen, Z. Hu, D. Yan, X. Zhou, G. Cui, *Nat. Commun.* **2019**, *10*, 5374.
- [21] J. N. C. Lopes, A. A. H. Padua, *Theor. Chem. Acc.* **2012**, *131*.
- [22] L. S. Doddia, I. Cabeza de Vaca, J. Tirado-Rives, W. L. Jorgensen, *Nucleic Acids Res.* **2017**, *45*, W331–W336.
- [23] L. Martínez, R. Andrade, E. G. Birgin, J. M. Martínez, *J. Comput. Chem.* **2009**, *30*, 2157–2164.
- [24] W. Smith, T. R. Forester, *J. Mol. Graphics* **1996**, *14*, 136–141.
- [25] M. Kar, B. Winther-Jensen, M. Forsyth, D. R. MacFarlane, *Phys. Chem. Chem. Phys.* **2014**, *16*, 10816–10822.
- [26] J. Ravi, A. E. Hills, E. Cerasoli, P. D. Rakowska, M. G. Ryadnov, *Eur. Biophys. J.* **2011**, *40*, 339–345.
- [27] T. J. Simons, P. C. Howlett, A. A. J. Torriero, D. R. MacFarlane, M. Forsyth, *J. Phys. Chem. C* **2013**, *117*, 2662–2669.
- [28] a) L. Garcia-Quintana, F. Chen, N. Ortiz-Vitoriano, Y. Zhang, L. A. O'Dell, D. R. MacFarlane, M. Forsyth, A. M. Bond, P. C. Howlett, C. Pozo-Gonzalo, *Batteries & Supercaps* **2021**, *4*, 513–521; b) P. Johansson, J. Grondin, J.-C. Lassègues, *J. Phys. Chem. A* **2010**, *114*, 10700–10705.
- [29] S. J. Archibald, *Comp. Coord. Chem. II* (Eds.: J. A. McCleverty, T. J. Meyer), Pergamon, Oxford **2003**, pp. 1147–1251.
- [30] M. Kar, D. R. MacFarlane, J. M. Pringle, *Fundamentals of Ionic Liquids: From Chemistry to Applications*, Wiley-VCH Verlag GmbH & Co. KGaA **2017**.
- [31] a) N. Sasaya, M. Matsumiya, K. Tsunashima, *Polyhedron* **2015**, *85*, 888–893; b) K. Periyapperuma, J. M. Pringle, L. Sanchez-Cupido, M. Forsyth, C. Pozo-Gonzalo, *Green Chem.* **2021**, *23*, 3410–3419.
- [32] a) Y. Tian, Y. An, C. Wei, H. Jiang, S. Xiong, J. Feng, Y. Qian, *Nano Energy* **2020**, *78*, 105344; b) S. A. Ferdousi, M. Hilder, A. Basile, H. Zhu, L. A. O'Dell, D. Saurel, T. Rojo, M. Armand, M. Forsyth, P. C. Howlett, *ChemSusChem* **2019**, *12*, 1700–1711.
- [33] a) Q. Li, A. Chen, D. Wang, Z. Pei, C. Zhi, *Joule* **2022**, *6*, 273–279; b) V. Bhaghavathi Parambath, Z. Zhao-Karger, T. Diermant, M. Jäckle, Z. Li, T. Scherer, A. Gross, R. Behm, M. Fichtner, *J. Mater. Chem. A* **2020**, *8*, 22998–23010.
- [34] a) J. Shi, K. Xia, L. Liu, C. Liu, Q. Zhang, L. Li, X. Zhou, J. Liang, Z. Tao, *Electrochim. Acta* **2020**, *358*, 136937; b) B. Raza, Y. Zhang, M. Xu, J. Yang, Y. NuLi, J. Wang, *Chem. Eng. J.* **2022**, *447*, 137496.
- [35] K. Sada, B. Senthilkumar, P. Barpanda, *J. Phys. Chem. A* **2019**, *7*, 23981–23988.
- [36] O. Galmiz, M. Stupavska, H. Wulff, H. Kersten, A. Brablec, M. Cernak, *Open Chemistry* **2015**, *13*, 198–203.
- [37] a) F. Kayaci, S. Vempati, I. Donmez, N. Biyikli, T. Uyar, *Nanoscale* **2014**, *6*, 10224–10234; b) R. Khokhra, B. Bharti, H.-N. Lee, R. Kumar, *Sci. Rep.* **2017**, *7*, 15032–15032.
- [38] B. Dilasari, Y. Jung, K. Kwon, *J. Ind. Eng. Chem.* **2017**, *45*, 375–379.
- [39] a) T. Belmonte, J. Thiébaut, D. Mezerette, *J. Phys. D* **2002**, *35*, 1919; b) F. Yin, J. Ren, Y. Zhang, T. Tan, Z. Chen, *Nanoscale Res. Lett.* **2018**, *13*, 307; c) L. Chen, Z. Hu, L. Liu, Y. Huang, *RSC Adv.* **2013**, *3*, 24664–24670.
- [40] H. Chen, G. Wei, X. Liang, P. Liu, Y. Xi, J. Zhu, *Catal. Sci. Technol.* **2020**, *10*, 5829–5839.
- [41] A. K.-V. Alexander V. Naumkin, Stephen W. Gaarenstroom, Cedric J. Powell, "NIST X-ray photoelectron spectroscopy database", can be found under <https://searchworks.stanford.edu/view/9742414> (accessed 2nd July, 2022).
- [42] M. Smith, L. Scudiero, J. Espinal, J.-S. McEwen, M. Garcia-Perez, *Carbon* **2016**, *110*, 155–171.
- [43] N. Togasaki, T. Momma, T. Osaka, *J. Power Sources* **2014**, *261*, 23–27.
- [44] Q. Yang, D. Wang, C. Wang, X. Li, K. Li, Y. Peng, J. Li, *Catal. Sci. Technol.* **2018**, *8*, 3166–3173.
- [45] a) M. C. Biesinger, L. W. M. Lau, A. R. Gerson, R. S. C. Smart, *Appl. Surf. Sci.* **2010**, *257*, 887–898; b) H. Liu, Q. Luo, J. Hu, L. Wei, W. Zhang, H. Zheng, S. Wu, K. Tang, *Chin. J. Chem.* **2022**, *40*, 2276–2284.
- [46] R. Al-Gaashani, S. Radiman, A. R. Daud, N. Tabet, Y. Al-Douri, *Ceram. Int.* **2013**, *39*, 2283–2292.
- [47] V. M. Badiani, C. Casadevall, M. Miller, S. J. Cobb, R. R. Manuel, I. A. C. Pereira, E. Reisner, *J. Am. Chem. Soc.* **2022**, *144*, 14207–14216.
- [48] I. Safo, C. Dosche, M. Özsalan, *ChemPhysChem* **2019**, *20*, 3010–3023.
- [49] D. Weingarth, I. Czekaj, Z. Fei, A. Foelske-Schmitz, P. J. Dyson, A. Wokaun, R. Kotz, *J. Electrochem. Soc.* **2012**, *159*, H611–H615.
- [50] S. Sinha, D. Choudhury, G. Rajaraman, S. K. Sarkar, *RSC Adv.* **2015**, *5*, 22712–22717.

Manuscript received: September 20, 2022

Revised manuscript received: October 19, 2022

Accepted manuscript online: October 26, 2022

Version of record online: November 23, 2022